

Measurement of inclusive π^0 production in the charged-current interactions of neutrinos in a 1.3-GeV wide band beam

C. Mariani,^{23,†} A. Tornero-Lopez,³¹ J. L. Alcaraz,¹ S. Andringa,¹ S. Aoki,¹⁴ Y. Aoyama,¹⁴ J. Argyriades,⁵ K. Asakura,¹⁴ R. Ashie,²⁸ F. Berghaus,³ H. Berns,³² H. Bhang,²⁴ A. Blondel,⁹ S. Borghi,^{9,‡} J. Bouchez,^{5,*} J. Burguet-Castell,³¹ D. Casper,⁴ J. Catala,³¹ C. Cavata,⁵ A. Cervera,^{9,§} S. M. Chen,³⁰ K. O. Cho,⁶ J. H. Choi,⁶ U. Dore,²³ X. Espinal,¹ M. Fechner,⁵ E. Fernandez,¹ Y. Fujii,¹¹ Y. Fukuda,¹⁹ J. Gomez-Cadenas,³¹ R. Gran,³² T. Hara,¹⁴ M. Hasegawa,^{16,||} T. Hasegawa,¹¹ Y. Hayato,²⁸ R. L. Helmer,³⁰ K. Hiraide,^{16,¶} J. Hosaka,²⁸ A. K. Ichikawa,¹⁶ M. Inuma,¹² A. Ikeda,²¹ T. Ishida,¹¹ K. Ishihara,²⁸ T. Ishii,¹¹ M. Ishitsuka,²⁹ Y. Itow,²⁸ T. Iwashita,¹¹ H. I. Jang,⁶ E. J. Jeon,²⁴ I. S. Jeong,⁶ K. K. Joo,²⁴ G. Jover Manas,¹ C. K. Jung,²⁶ T. Kajita,²⁹ J. Kameda,²⁸ K. Kaneyuki,²⁹ I. Kato,³⁰ E. Kearns,² C. O. Kim,¹⁵ M. Khabibullin,¹³ A. Khotjantsev,¹³ D. Kielczewska,^{33,25} J. Y. Kim,⁶ S. B. Kim,²⁴ P. Kitching,³⁰ K. Kobayashi,²⁶ T. Kobayashi,¹¹ A. Konaka,³⁰ Y. Koshio,²⁸ W. Kropp,⁴ Yu. Kudenko,¹³ Y. Kuno,²² Y. Kurimoto,^{16,||} T. Kutter,^{17,3} J. Learned,¹⁰ S. Likhoded,² I. T. Lim,⁶ P. F. Loverre,²³ L. Ludovici,²³ H. Maesaka,^{16,**} J. Mallet,⁵ S. Matsuno,¹⁰ V. Matveev,¹³ K. McConnel Mahn,^{18,††} C. McGrew,²⁶ S. Mikheyev,¹³ A. Minamino,²⁸ S. Mine,⁴ O. Mineev,¹³ C. Mitsuda,²⁸ M. Miura,²⁸ Y. Moriguchi,¹⁴ S. Moriyama,²⁸ T. Nakadaira,¹¹ M. Nakahata,²⁸ K. Nakamura,¹¹ I. Nakano,²¹ T. Nakaya,¹⁶ S. Nakayama,²⁹ T. Namba,²⁸ R. Nambu,²⁸ S. Nawang,¹² K. Nishikawa,¹¹ K. Nitta,^{16,‡‡} F. Nova,¹ P. Novella,³¹ Y. Obayashi,²⁸ A. Okada,²⁹ K. Okumura,²⁹ S. M. Oser,³ Y. Oyama,¹¹ M. Y. Pac,⁷ F. Pierre,^{5,*} A. Rodriguez,¹ C. Saji,²⁹ M. Sakuda,²¹ F. Sanchez,¹ K. Scholberg,⁸ R. Schroeter,⁹ M. Sekiguchi,¹⁴ M. Shiozawa,²⁸ K. Shiraishi,³² G. Sitjes,³¹ M. Smy,⁴ H. Sobel,⁴ M. Sorel,³¹ J. Stone,² L. Sulak,² A. Suzuki,¹⁴ Y. Suzuki,²⁸ M. Tada,¹¹ T. Takahashi,¹² Y. Takenaga,²⁹ Y. Takeuchi,²⁸ K. Taki,²⁸ Y. Takubo,²² N. Tamura,²⁰ M. Tanaka,¹¹ R. Terri,²⁶ S. T'Jampens,⁵ Y. Totsuka,¹¹ M. Vagins,⁴ C. W. Walter,⁸ W. Wang,² R. J. Wilkes,³² L. Whitehead,²⁶ S. Yamada,²⁸ Y. Yamada,¹¹ S. Yamamoto,^{16,§§} C. Yanagisawa,²⁶ N. Yershov,¹³ H. Yokoyama,²⁷ M. Yokoyama,¹⁶ J. Yoo,²⁴ M. Yoshida,²² and J. Zalipska²⁵

(The K2K Collaboration)

¹*Institut de Fisica d'Altes Energies, Universitat Autònoma de Barcelona, E-08193 Bellaterra (Barcelona), Spain*

²*Department of Physics, Boston University, Boston, Massachusetts 02215, USA*

³*Department of Physics & Astronomy, University of British Columbia, Vancouver, British Columbia V6T 1Z1, Canada*

⁴*Department of Physics and Astronomy, University of California, Irvine, Irvine, California 92697-4575, USA*

⁵*Commissariat à l'Énergie Atomique et aux Énergies Alternatives, Centre de Saclay, IRFU/SPP, 91191 Gif-sur-Yvette, France*

⁶*Department of Physics, Chonnam National University, Kwangju 500-757, Korea*

⁷*Department of Physics, Dongshin University, Naju 520-714, Korea*

⁸*Department of Physics, Duke University, Durham, North Carolina 27708, USA*

⁹*DPNC, Section de Physique, University of Geneva, CH1211, Geneva 4, Switzerland*

¹⁰*Department of Physics and Astronomy, University of Hawaii, Honolulu, Hawaii 96822, USA*

¹¹*High Energy Accelerator Research Organization (KEK), Tsukuba, Ibaraki 305-0801, Japan*

¹²*Graduate School of Advanced Sciences of Matter, Hiroshima University, Higashi-Hiroshima, Hiroshima 739-8530, Japan*

¹³*Institute for Nuclear Research, Moscow 117312, Russia*

¹⁴*Kobe University, Kobe, Hyogo 657-8501, Japan*

¹⁵*Department of Physics, Korea University, Seoul 136-701, Korea*

¹⁶*Department of Physics, Kyoto University, Kyoto 606-8502, Japan*

¹⁷*Department of Physics and Astronomy, Louisiana State University, Baton Rouge, Louisiana 70803-4001, USA*

¹⁸*Department of Physics, Massachusetts Institute of Technology, Cambridge, Massachusetts 02139, USA*

¹⁹*Department of Physics, Miyagi University of Education, Sendai 980-0845, Japan*

²⁰*Department of Physics, Niigata University, Niigata, Niigata 950-2181, Japan*

*Deceased.

†Present Address: Department of Physics, Columbia University, New York, NY 10027, USA.

‡Present Address: School of Physics and Astronomy, University of Glasgow, Glasgow, United Kingdom.

§Present Address: Instituto de Fisica Corpuscular, Universidad de Valencia, Valencia, Spain.

||Present Address: High Energy Accelerator Research Organization (KEK), Tsukuba, Ibaraki 305-0801, Japan.

¶Present Address: Kamioka Observatory, Institute for Cosmic Ray Research, University of Tokyo, Kamioka, Gifu 506-1205, Japan.

**Present Address: XFEL Project Head Office, RIKEN, Sayo, Hyogo 671-5148, Japan.

††Present Address: TRIUMF, Vancouver, British Columbia V6T 2A3, Canada.

‡‡Present Address: National Institute of Radiological Sciences (NIRS), Chiba-shi 263-8555, Japan.

§§Present Address: The University of Tokyo, International Center for Elementary Particle Physics, Hongo, Tokyo 113-0033, Japan.

²¹*Department of Physics, Okayama University, Okayama, Okayama 700-8530, Japan*²²*Department of Physics, Osaka University, Toyonaka, Osaka 560-0043, Japan*²³*University of Rome Sapienza and INFN, I-00185 Rome, Italy*²⁴*Department of Physics, Seoul National University, Seoul 151-747, Korea*²⁵*A. Soltan Institute for Nuclear Studies, 00-681 Warsaw, Poland*²⁶*Department of Physics and Astronomy, State University of New York, Stony Brook, New York 11794-3800, USA*²⁷*Department of Physics, Tokyo University of Science, Noda, Chiba 278-0022, Japan*²⁸*Kamioka Observatory, Institute for Cosmic Ray Research, University of Tokyo, Kamioka, Gifu 506-1205, Japan*²⁹*Research Center for Cosmic Neutrinos, Institute for Cosmic Ray Research, University of Tokyo, Kashiwa, Chiba 277-8582, Japan*³⁰*TRIUMF, Vancouver, British Columbia V6T 2A3, Canada*³¹*Instituto de Física Corpuscular, E-46071 Valencia, Spain*³²*Department of Physics, University of Washington, Seattle, Washington 98195-1560, USA*³³*Institute of Experimental Physics, Warsaw University, 00-681 Warsaw, Poland*

(Received 8 December 2010; published 16 March 2011)

In this paper, we report on the measurement of the rate of inclusive π^0 production induced by charged-current neutrino interactions in a C_8H_8 target at a mean energy of 1.3 GeV in the K2K near detector. Out of a sample of 11 606 charged-current neutrino interactions, we select 479 π^0 events with two reconstructed photons. We find that the cross section for the inclusive π^0 production relative to the charged-current quasielastic cross section is $\frac{\sigma_{CC\pi^0}}{\sigma_{CCQE}} = 0.426 \pm 0.032$ (stat) ± 0.035 (syst). The energy-dependent cross section ratio is also measured. The results are consistent with previous experiments for exclusive channels on different targets.

DOI: [10.1103/PhysRevD.83.054023](https://doi.org/10.1103/PhysRevD.83.054023)

PACS numbers: 13.85.Ni, 13.85.Qk

I. INTRODUCTION

After the observation of solar neutrino and atmospheric neutrino oscillations [1–7] and their confirmation, respectively, at reactors [8] and accelerators [9], the primary aim of current and future neutrino experiments is to measure the θ_{13} mixing angle and to improve accuracy in the measurement of oscillation parameters. One of the largest limitations of accelerator-based neutrino experiments comes from the poor experimental knowledge of neutrino cross sections in the GeV energy range. Concerning the measurement of θ_{13} via subleading $\nu_\mu \rightarrow \nu_e$ oscillation searches, one of the main backgrounds to the ν_e signal comes from ν_μ neutral-current (NC) interactions producing π^0 's. Experimental input on the rate of the related charged-current (CC) channel, which is the focus of this paper, and measurement of the π^0 production momentum spectrum, allow better understanding of this background. Concerning the improvements in the measurement of oscillation parameters and, in particular, of the atmospheric mixing angle θ_{23} and mass-squared difference Δm_{23}^2 via the measurement of the distortion of the neutrino energy spectrum induced by neutrino oscillations, knowledge of the overall yield and interaction-type composition of CC inelastic interactions is crucial. This is because the reconstruction of neutrino energy in CC interactions via kinematic means is less accurate in inelastic interactions, compared to quasielastic (CC QE) interactions. Charged-current inclusive π^0 production (CC π^0) constitutes a large component of all CC inelastic interactions. In addition, since uncertainties in the nuclear models play a significant

role in the neutrino-nucleus cross section, it is important to have measurements on different target materials.

Although there are several theoretical approaches to model these processes, the experimental constraints are rather weak. Very little data exists in the few-GeV neutrino energy range. Experimental measurements of neutral-pion production via CC interactions of few-GeV neutrinos on deuterium have been collected in the past for single-pion [10–13] and two-pion [14] final states. At higher energies, CC single- π^0 production cross sections have been measured on deuterium [15] and heavy freon [16] targets.

In this paper, we present the measurement of inclusive CC neutrino interactions with a π^0 in the final state made with the KEK to Kamioka (K2K) scintillator-bar tracker/electromagnetic calorimeter (SciBar/EC) detector system. The measurement presented here is the first result on a carbon target in the few-GeV neutrino energy range and improves the precision of previous results on different targets. First, we obtain the cross section for this process with respect to the cross section for both CC QE and inelastic interactions. We quote our result as a cross section ratio rather than as an absolute cross section, in order to reduce the impact of large uncertainties in the estimation of the K2K neutrino flux affecting the SciBar detector. Second, by reconstructing the neutrino energy of CC interactions resulting in inclusive π^0 production, we present the energy dependence of this cross section ratio. Third, by using previous K2K experimental input on CC single-pion production [17], we interpret our result as a measurement of the CC deep inelastic cross section, relative to the CC

QE cross section. Fourth, we present relevant π^0 production kinematic distributions of our $CC\pi^0$ candidate events.

The paper is organized as follows: Sec. II describes the experimental setup, the neutrino beam and the neutrino near detector at KEK; Sec. III describes the simulation of the experiment, focusing on the neutrino interaction simulation. In Sec. IV, we discuss the ingredients of our main cross section analysis, describing the experimental signature, the CC event selection, the photon selection, the π^0 mass, and the neutrino energy reconstruction; Sec. V describes our likelihood fit method; Sec. VI describes the systematic uncertainties affecting our measurement; Sec. VII presents the energy-dependent and energy-independent cross section results, and the comparison with the neutrino interaction simulation and with existing results is given in Sec. VIII. Conclusions are given in Sec. VIII.

II. EXPERIMENTAL SETUP

A. Neutrino beam

The K2K experiment [9,18–20] is a long-baseline neutrino oscillation experiment in which a beam of muon neutrinos created at KEK is detected 250 km away in the Super-Kamiokande detector, located in Kamioka, Japan. To produce the neutrino beam, protons are accelerated by the KEK proton synchrotron to a kinetic energy of 12 GeV and then extracted every 2.2 s in a single turn to the neutrino beam line. The duration of an extraction, or spill, is 1.1 μ s, and each spill contains 9 bunches of protons at a 125-ns time interval. The protons are steered to the neutrino beam line to strike an aluminum target, producing secondary particles. Two toroidal magnetic horns focus the positively charged particles, mainly π^+ 's, in the forward direction. The focused positive pions are allowed to decay into a 200-m-long tunnel, where they produce neutrinos via $\pi^+ \rightarrow \mu^+ \nu_\mu$. A beam absorber made of iron, concrete, and soil is located at the end of the decay volume to stop all particles except neutrinos. The direction and intensity of the neutrino beam are checked spill-by-spill, by monitoring the muons produced by pion decay. The energy spectrum of the neutrino beam is checked by occasionally monitoring the pions focused by the horn magnets

Over the duration of the K2K experiment, a total of 9.2×10^{19} protons was delivered to the target to generate the neutrino beam. The SciBar and EC detectors took data from October 2003 until November 2004; 2.02×10^{19} protons on target were accumulated during this time.

A Monte Carlo (MC) simulation is used to predict the properties of the neutrino beam. According to the simulation, the beam at the near detector is about 97.3% pure ν_μ , with a mean energy of 1.3 GeV. A fit of data of neutrino interactions in all the near detectors is used to fine-tune the simulated neutrino energy spectrum [9]. Figure 1 shows the energy spectrum for all muon-neutrino interactions in the fiducial volume of the SciBar detector.

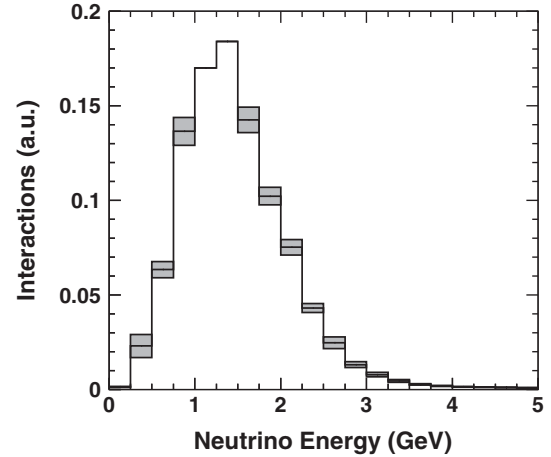


FIG. 1. The energy spectrum for all muon neutrino interactions in the SciBar fiducial volume. The gray boxes correspond to the shape systematic uncertainty.

B. Neutrino detectors at KEK

The near detector system is located 300 m downstream of the proton target. The purpose of the near detector is to measure the direction, flux, and energy spectrum of neutrinos at KEK before oscillation. The near detector is also used for measurements of neutrino cross sections.

A schematic view of the near detector is shown in Fig. 2. The near detector consists of a 1-kt water Čerenkov detector [21], a scintillating-fiber/water target tracker [22], a fully active SciBar complemented by a lead and fibers EC, and a muon range detector (MRD). In this section, we describe the SciBar, EC, and MRD, since data taken from these detectors are used in the present analysis. A full description of the K2K near detectors can be found in [9].

1. SciBar

The SciBar detector acts as a fully active neutrino target, and its primary role is to reconstruct the neutrino interaction vertex and detect the final-state charged particles.

SciBar [23,24] consists of 14 848 extruded scintillator bars of $1.3 \times 2.5 \times 300$ cm³. Groups of 116 bars are arranged horizontally or vertically to make one plane. The planes are arranged in 64 layers orthogonal to the beam, each consisting of one horizontal and one vertical plane. The total volume is 3 m \times 3 m \times 1.7 m, for a total mass of \sim 15 tons. Figure 3 shows a diagram of the SciBar detector.

The extruded scintillator bars are produced by FNAL [25]. The bars are made of polystyrene (C₈H₈), 2,5-diphenyloxazole (1%), and 1,4-bis(5-phenyl-2-oxazolyl) benzene (0.03%). Each bar is 1.3 cm \times 2.5 cm \times 300 cm and has a 0.25-mm-thick reflective coating made of TiO₂. The peak of the emission spectrum for the scintillator is at 420 nm. A 1.5-mm-diameter wavelength-shifting (WLS) fiber [Kuraray Y11(200)MS] is inserted in a 1.8-mm hole in each bar to guide the scintillation light to multianode photomultiplier tubes (MAPMTs). The average attenuation

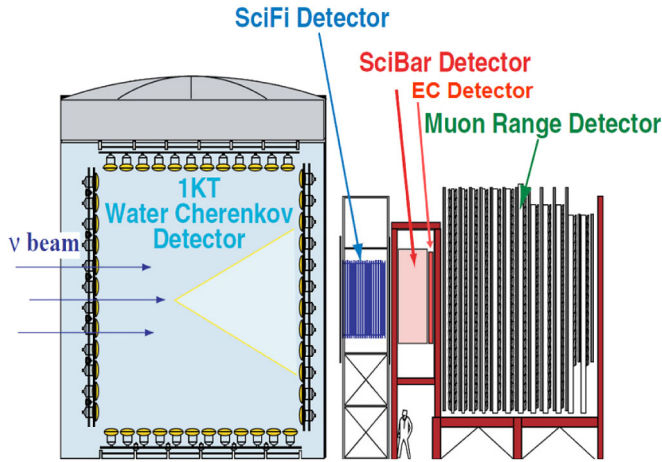


FIG. 2 (color online). Schematic view of the near neutrino detector.

length of the WLS fibers is approximately 350 cm. The absorption peak for the fibers is at 430 nm (matching the emission peak for the scintillator), and the emission peak is at 476 nm. The scintillation light produced is detected by Hamamatsu H8804 MAPMTs. Each MAPMT has 64 channels arranged in an 8×8 array. Each pixel is $2 \text{ mm} \times 2 \text{ mm}$. The cathode material is Bialkali, with a quantum efficiency of 21% at a wavelength of 390 nm. The cathode is sensitive to wavelengths between 300 and 650 nm. A typical channel gain is 6×10^5 at a supply voltage of 800–900 V. The basic properties, such as gain and linearity, are measured for each channel before installation. The nonlinearity of the output signal vs input charge is

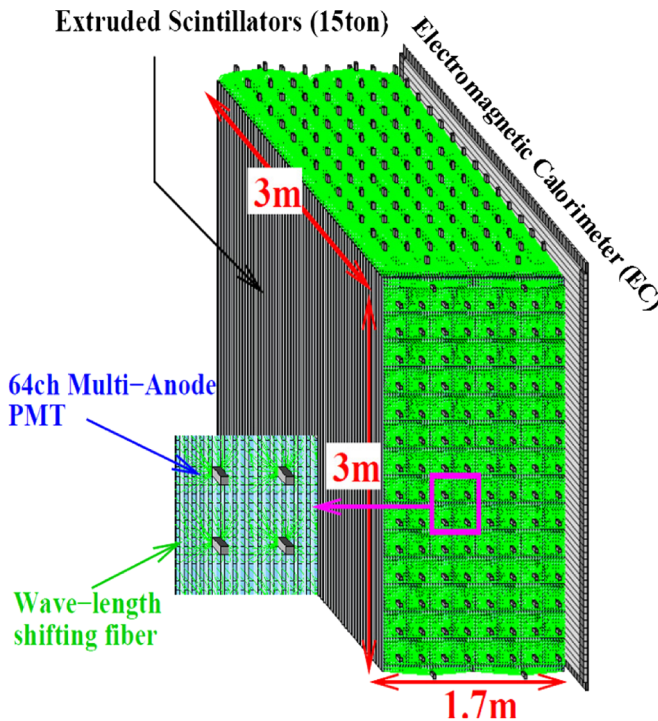


FIG. 3 (color online). Diagram of SciBar and of the EC.

5% at 200 photoelectrons (p.e.) at a gain of 5×10^5 . Cross talk in the MAPMT is approximately 3% in neighboring channels. Groups of 64 fibers are bundled together and glued to an attachment to be precisely aligned with the pixels of the MAPMT. SciBar's readout system [26] consists of a front-end electronics board (FEB) attached to each MAPMT and a back-end Versa Module Eurocard (VME) module. The front-end electronics board uses Viking-architecture chip/trigging-architecture chip (VA/TA) application-specific integrated circuits (ASICs). The VA is a 32-channel preamplifier chip with a shaper and multiplexer. The TA provides timing information by taking the OR of 32 channels. Each FEB uses two VA/TA packages to read 64 analog signals and two timing signals for each MAPMT. Each back-end VME board controls the readout of eight FEBs. Flash analog-to-digital converters are used to digitize the charge information, and time-to-digital converters are used to process the timing information. The pedestal width is approximately 0.3 p.e., and the timing resolution is 1.3 ns. In order to monitor and correct for gain drift during operation, SciBar is equipped with a gain calibration system using light-emitting diodes [27]. The system shows that the gain is stable within 5% for the entire period of operation. Cosmic-ray data collected between beam spills are used to calibrate the light yield of each channel. The average light yield per bar is approximately 20 p.e. for a minimum ionizing particle. The light yield is stable within 1% for the whole period of operation. Pedestal, light-emitting-diode, and cosmic-ray data are taken simultaneously with beam data. A cross talk correction is applied to both data and MC before event reconstruction [17]. After the cross talk correction, scintillator strips with a pulse height larger than 2 p.e. (corresponding to about 0.2 MeV) are selected for tracking. Charged particles are reconstructed by looking for track projections in each of the two-dimensional views ($x-z$ and $y-z$) using a cellular automaton algorithm [28]. Three-dimensional tracks are reconstructed by matching the z edges and timing information of the 2D tracks. Reconstructed tracks are required to have hits in at least 3 consecutive layers. The minimum length of a reconstructible track is, therefore, 8 cm, which corresponds to a momentum threshold of 450 MeV/ c for protons. The reconstruction efficiency for an isolated track longer than 10 cm is 99%. The efficiency is lower for multiple-track events due to the overlapping of tracks in one or both views.

2. EC

The EC detector is an electromagnetic calorimeter installed just downstream of SciBar, as shown in Fig. 3. The main purpose of the EC is the longitudinal containment of the electromagnetic showers, since the whole SciBar corresponds to only 4 radiation lengths. The EC provides 11 radiation lengths and has 85% energy containment at 3 GeV. The EC consists of one plane of 30 horizontal

modules and one plane of 32 vertical modules. The two planes have a cross sectional area of $2.7 \text{ m} \times 2.6 \text{ m}$ and $2.6 \text{ m} \times 2.5 \text{ m}$, respectively. The modules were originally made for the CHORUS neutrino experiment at CERN [29]. Each module is a sandwich of lead and scintillating fibers, built by piling up extruded sheets of grooved lead with scintillating fibers positioned in the grooves. A module consists of a stack of 21 lead sheets, 2650 mm long, and 740 fibers of 1-mm diameter and 3050 mm long. The groove diameter is 1.1 mm, and the sheet thickness is 1.9 mm. The sheet's material is 99% lead with 1% antimony content to improve its mechanical properties. The stack is kept together by a welded steel case. An overall thickness nonuniformity of less than 2% was achieved through the extrusion process. At both ends, fibers are bundled in two independent groups, defining two different readout cells of about $42 \times 42 \text{ mm}^2$ transverse cross section. The fibers are manufactured by Kuraray (type SCSF81) and consist of a polystyrene core surrounded by a $30 \text{ }\mu\text{m}$ thick acrylic cladding, with an emission maximum in the blue, around 420 nm. To improve the light collection uniformity, an acrylic black paint is applied on the surface of the last 5 cm of fibers on each side. This has the effect of reducing the light coming from the cladding, which has a smaller attenuation length. In addition, in order to select the spectral component with a larger attenuation length, a yellow filter (Kodak Wratten No. 3) is used. The attenuation length was measured to be $(462 \pm 53) \text{ cm}$ when the modules were built [29] and was recently measured to be $(400 \pm 12) \text{ cm}$. At both ends of the readout cell, fibers are grouped into two bundles of hexagonal cross section (22.2 mm apex to apex) and are coupled to a Plexiglas light guide, also with hexagonal cross section (24 mm apex to apex). The hexagonal shape and the length of the light guide were chosen to reduce disuniformities in the mixing of the light coming out of the individual fibers [30]. The light guides are coupled to 1–1/8 inch diameter photomultipliers, type R1355/SM from Hamamatsu, with a special green extended photocathode of 25-mm effective diameter. The cathode material is Bi-alkali, with a quantum efficiency of 27% in the wavelength range 350–450 nm. The cathode is sensitive to wavelengths from 300 to 650 nm. A typical current amplification is 2.1×10^6 at the supply voltage of 1600 V. The anode dark current is 10 nA. The photomultiplier tube (PMT) gain of each channel was measured before installation. The nonlinearity of the output signal vs input charge is 2% at 60 mA (corresponding to 600 photoelectrons) at a gain of 2×10^6 . The PMT produces a differential signal using the outputs of the cathode and the last dynode. Signals are read via multipolar differential screened cables, 100 m long. The readout system consists of an 8-charge-to-digital-converter VME (CAEN V792) with a 32-channel 12-bit analog-to-digital converter. Impedance matching cards (CAEN A992 custom-modified) are used to convert

the differential signals into single-ended signals and to decouple the PMTs and the charge-to-digital-converter grounds. Cosmic rays measured during normal data taking in between the neutrino spills are used to calibrate the detector and to monitor the gain stability. After the calibration, the spread in the individual channel response was stable within 1%. The pedestal width is approximately 0.7 photoelectrons, and the energy resolution was measured in a test beam as $14\%/\sqrt{E(\text{GeV})}$. The energy deposited is reconstructed by searching for clusters of nearby hits above the threshold. In this analysis, clusters are reconstructed, searching for hits with more than 20 MeV in the vertical plane and 10 MeV in the horizontal plane. Hits in the nearest counters are iteratively added to the cluster if their energy is greater than 10 MeV (5 MeV) for the vertical (horizontal) plane. The cluster position is the energy-weighted average of the positions of the counters belonging to the cluster.

3. MRD

The MRD [31] is the most downstream detector. It consists of 12 layers of iron between 13 layers of vertical and horizontal drift tubes. Each layer is approximately $7.6 \text{ m} \times 7.6 \text{ m}$. To have good energy resolution over the entire energy spectrum, the four upstream iron layers are each 10 cm thick, while the other eight planes are 20 cm thick. The total iron thickness of 2 m covers muon energies up to 2.8 GeV, which corresponds to 95% of all the muons produced by neutrino interactions in the K2K. There are 6632 aluminum drift tubes filled with P10 gas (Ar:CH₄ = 90%:10%). The total mass of the iron is 864 tons, and the mass of the drift tubes is 51 tons. The MRD is used to monitor the stability of the neutrino beam direction, profile, and spectrum by measuring the energy, angle, and production point of muons produced by CC neutrino interactions in the iron target. The MRD is also used to identify muons produced in the upstream detectors. The energy and angle of the muon can be measured by the combination of the MRD and the other fine-grained detectors. It is necessary to measure the muon energy and direction in order to reconstruct the energy of the incident neutrino for CC events. The MRD tracking efficiency is 66, 95, and 97.5% for tracks that traverse one, two, and three iron layers, respectively; for longer tracks, the efficiency approaches 99%. A track that hits less than three layers of MRD is called a “one-layer hit” (MRD1L), while a track that hits more than three iron layers will be reconstructed as a 2D track in $x-z$ or $y-z$ planes. The 2D-track pair which has the longest overlap is taken as a 3D track (MRD3D). The range of a track is estimated using the path length of the reconstructed track in iron. The muon energy is calculated by the range of the track. The uncertainty in the muon energy due to differences among various calculations of the relationship between muon energy and range is 1.7%. The uncertainty in the weight

of the iron is 1%. Thus, the systematic error in the MRD energy scale is quoted as the sum of these uncertainties, 2.7%. The energy resolution is estimated by Monte Carlo simulation to be 0.12 GeV for forward-going muons. The angular resolution is about 5 degrees.

III. SIMULATION

A. Neutrino interactions

The neutrino interaction simulation plays an important role for estimating the event yields and the topological and kinematical properties for CC neutrino interactions in SciBar producing neutral pions, as well as for background processes. We use the NEUT program library to simulate neutrino interactions with protons and carbon nuclei within the SciBar detector material. NEUT [32] simulates neutrino interactions over a wide energy range, from ~ 100 MeV up to TeV neutrino energies, and on different nuclear targets.

In the simulation program, the following CC and NC neutrino interactions are considered: QE scattering ($\nu N \rightarrow lN'$), single-pion production ($\nu N \rightarrow lN'm$), coherent π production ($\nu^{12}\text{C} \rightarrow l\pi^{12}\text{C}$), and deep inelastic scattering (DIS, $\nu N \rightarrow lN' \text{hadrons}$). In these reactions, N and N' are the nucleons (proton or neutron), l is the lepton (either a charged lepton or a neutrino), and m is a meson. If the neutrino interaction occurs in a carbon nucleus, the interactions of the generated particles with the remaining nucleons of the nucleus are also simulated.

The total charged-current cross section predicted by NEUT, together with the QE scattering, single-pion production, and deep inelastic scattering contributions, are shown in Fig. 4, overlaid with data from several experiments.

Given the K2K beam neutrino energy spectrum, Table I shows the fraction of interactions in SciBar that are expected to be QE, single-pion, etc., according to the simulation.

1. π^0 -producing charged-current neutrino interactions

For the simulation of CC neutrino interactions resulting in inclusive π^0 production, we adopt distinct models, depending on the invariant mass W of the hadronic system in the final state and on the pion multiplicity. A summary of the models used to simulate the cross section and the final-state kinematics is given in Table II, while more details are given in the text below.

For $W < 2$ GeV and production of single π^0 's and no other pions (charged or neutral), we use the resonance-mediated Rein-Sehgal model [33]. In this model, the interaction simulation is performed via a two-step process. First, the neutrino-induced excitation of the baryon resonance N^* is modeled:

$$\nu_\mu + n \rightarrow \mu^- + N^*,$$

which is then followed by the resonance decay to a pion-nucleon final state:

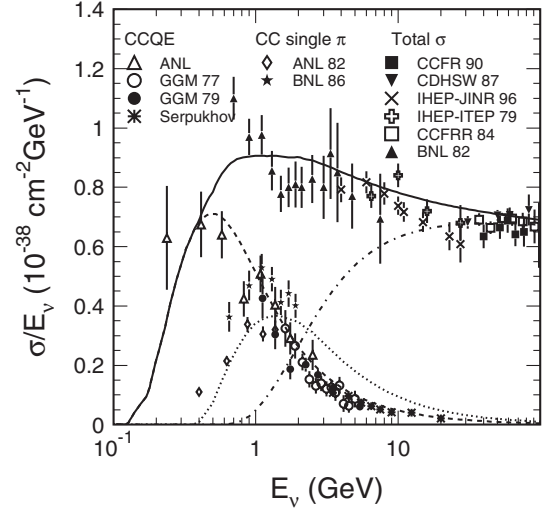


FIG. 4. Charged-current total cross section divided by the neutrino energy E_ν for neutrino-nucleon charged-current interactions [32]. The solid line shows the calculated total cross section. The dashed, dotted, and dash-dotted lines show the calculated quasielastic, single-pion, and deep inelastic scattering, respectively. The data points are taken from the following experiments: (Δ) ANL [51]; (\circ) GGM77 [52]; (\bullet) GGM79 [53], [59]; ($*$) Serpukhov [54]; (\diamond) ANL82 [11]; (\star) BNL86 [12]; (\blacksquare) CCFR90 [60]; (\blacktriangledown) CDHSW87 [61]; (\times) IHEP-JINR96 [62]; ($+$) IHEP-ITEP79 [63]; (\square) CCFRR84 [64]; and (\blacktriangle) BNL82 [65].

$$N^* \rightarrow \pi^0 + p.$$

The same $\pi^0 - p$ final state can be fed by several resonances. All baryon resonances with $W < 2$ GeV/ c^2 are taken into account with their corresponding resonance width and including possible interferences among them. Single- K and η productions are simulated by using the same framework as for the dominant single- π production processes. The model contains a phenomenological parameter (the single-pion axial-vector mass, M_A) that must be determined experimentally. As the value of M_A increases, interactions with higher Q^2 values (and, therefore, larger scattering angles) are enhanced. The M_A parameter in our resonance-mediated Rein-Sehgal model is set to 1.1 GeV/ c^2 . To determine the final-state kinematics in the decay of the dominant resonance $P_{33}(1232)$,

TABLE I. Expected neutrino interactions in SciBar.

Interaction type	Percent of Total
CC	71.8%
$\nu_\mu n \rightarrow \mu^- p$ (QE)	32.2%
$\nu_\mu p \rightarrow \mu^- p \pi^+$	18.0%
$\nu_\mu n \rightarrow \mu^- n \pi^+$	6.2%
$\nu_\mu n \rightarrow \mu^- p \pi^0$	5.0%
DIS	6.8%
Others (K and η)	3.6%
NC	28.2%

TABLE II. Models used to simulate the cross section and final-state kinematics for CC-inclusive π^0 production. In the table, W stands for the invariant mass of the final-state hadronic system, N and N' for nucleons, π for at least one charged or neutral pion, and X for any meson (including none). See text for details.

W (GeV/ c^2)	Process	Cross Section	Final-State Kinematics
<2.0	$\nu_\mu n \rightarrow \mu^- p \pi^0$	[33]	[34], isotropic
$1.3-2.0$	$\nu_\mu N \rightarrow \mu^- N' \pi^0 \pi$	[35,36]	[37]
>2.0	$\nu_\mu N \rightarrow \mu^- N' \pi^0 X$	[35,36]	[38]

Rein's method [34] is used to generate the pion angular distribution in the resonance rest frame. For the other resonances, the directional distribution of the generated pion is set to be isotropic in the resonance rest frame. The pion angular distribution for the related $\nu p \rightarrow \mu^- p \pi^+$ mode has been measured [12], and the results agree well with our model. To describe nucleons bound in carbon nuclei, nucleons are treated as quasifree particles in motion, using a relativistic Fermi gas model [39,40] with 225 MeV/ c Fermi surface momentum and assuming a nuclear binding energy of 27 MeV. The Pauli blocking effect in the decay of the baryon resonance is taken into account by requiring that the momentum of the nucleon should be larger than the Fermi surface momentum. In addition, pionless decay for the dominant Δ resonance ($\Delta N \rightarrow NN$) is considered. In this case, which is expected to occur with a 20% probability, no pion is present in the final state; only a lepton and a nucleon are emitted [41].

For the production of π^0 's in association with other pions (charged or neutral), the deep inelastic scattering cross section formalism, combined with GRV94 parton distribution functions [35], is used. Additionally, we have included the corrections in the small Q^2 region developed by Bodek and Yang [36]. For the simulation of DIS final-state kinematics in which the hadronic invariant mass, W , is larger than 2 GeV/ c^2 , we use the PYTHIA/JETSET library [38]. For $W < 2$ GeV/ c^2 , we use a custom-made program [37], based on data-driven average pion multiplicities and Kob-Nielsen-Olensen scaling. In the latter case, the multiplicity of pions is required to be larger than 1, because single-pion production is already taken into account by the resonance-mediated single-pion production.

2. Other neutrino interactions

Resonance-mediated single-pion production and deep inelastic scattering CC processes that do not result in the production of π^0 's, but possibly in the production of other mesons such as π^\pm , are also simulated according to the models described in Sec. III A 1. The same models are used, as well, to simulate the corresponding NC channels.

The formalism of CC and NC QE scattering off free nucleons used in the simulation is described by Llewellyn-Smith [42]. There is only one parameter in the model to be determined experimentally, the QE axial-vector mass, M_A . As for single-pion production via baryon

resonances, M_A is set to 1.1 GeV/ c^2 in our simulation, based on near detector data [19].

Coherent single-pion production—that is, the interaction between a neutrino and the entire carbon nucleus, resulting in the production of single pions and no nuclear breakup—is simulated using the formalism developed by Rein and Sehgal [43]. The coherent pion production axial-vector mass is set to 1.0 GeV/ c^2 in our model. Only neutral-current coherent pion production interactions are considered, because the cross section of the CC coherent pion production was found to be very small at K2K beam energies [44].

3. Intranuclear hadronic interactions

The intranuclear interactions of the mesons and nucleons produced in neutrino interactions with carbon nuclei are also important for this analysis. Because of the propagation in the nuclear matter of the target nucleus, the final-state particles observed differ from the one produced at the weak interaction vertex. Particles' absorption or production, as well as changes in the direction or momentum, affect the event classification. For example, π^0 's produced at the weak interaction vertex can be absorbed via intranuclear interactions within the target nucleus, therefore escaping direct detection. Likewise, intranuclear interactions can result in π^0 production within the target nucleus, even in the absence of π^0 's at the weak interaction vertex. Therefore, the interactions of pions, kaons, etas, and nucleons are also taken into account. The meson and nucleon interactions are treated using a cascade model, and each of the particles is traced in the nucleus until escaping from it.

In our simulation, the following intranuclear pion interactions are considered: inelastic scattering, charge exchange, and absorption. The actual procedure to simulate these interactions is the following: first, the generated position of the pion in the nucleus is set according to the Woods-Saxon nucleon density distribution [45]. Then, the interaction mode is determined by using the calculated mean free path of each interaction. To calculate these mean free paths, we adopt the model described by Salcedo *et al.* [46]. The calculated mean free paths depend not only on the momentum of the pion, but also on the position of the pion in the nucleus. If inelastic scattering or charge exchange occurs, the direction and momentum of the pion is determined by using the results of a phase shift

analysis obtained from $\pi - N$ scattering experiments [47]. When calculating the pion scattering amplitude, the Pauli blocking effect is also taken into account by requiring the nucleon momentum after the interaction to be larger than the Fermi surface momentum at the interaction point. This pion interaction simulation is tested by comparison with data, including $\pi^{12}\text{C}$ scattering and pion photoproduction ($\gamma + {}^{12}\text{C} \rightarrow \pi^- + X$) data.

Reinteractions of the nucleons (protons, neutrons) produced in the neutrino interaction are also important. Each nucleon-nucleon interaction modifies the nucleon momentum and direction, possibly causing the number of visible nucleons to be mispredicted if not properly modeled [48]. Elastic scattering and single- and two-pion production are considered.

Our simulation predicts that, in 26% of SciBar CC interactions with π^0 production at the primary neutrino-nucleon electroweak vertex, the neutral pion(s) does not escape the target nucleus. On the other hand, 15% of the events with π^0 emerging from the target nucleus are produced in nuclear interactions.

B. Detector response

The GEANT3 [49] package is used to simulate the detector geometry and the interactions and tracking of particles. The CALOR program library [50] is used to simulate the interactions of pions with the detector material for pions with momentum greater than $0.5 \text{ GeV}/c$. For lower-energy pions, a custom library [37] is used.

The energy loss of a particle in each single SciBar strip and each individual EC sensitive fiber is simulated. The energy deposition is converted in the detector response, taking into account the Birk's saturation of the scintillator, the light attenuation along the fibers, the Poisson fluctuation of the number of photoelectrons, the PMT resolution, and the electronic noise. The cross talk in nearby SciBar channels is also taken into account.

In SciBar, the timing of each hit is simulated from the true time of the corresponding energy deposition, corrected by the travel time of the light in the WLS fiber and smeared by the timing resolution.

The MRD simulation includes both ionization and multiple scattering in the drift chambers.

The input parameters of the detector simulation are derived from laboratory measurements and calibration data. The features of the simulation have been systematically compared and tuned with cosmic-ray and neutrino data.

IV. EXPERIMENTAL SIGNATURE

A. Definition of signal and background

In this analysis, the process we want to measure is defined inclusively with respect to a π^0 produced in the target nucleus of the CC neutrino interaction. We call an

event a signal event when it has one (or more) π^0 that comes from the neutrino interaction vertex or from a reinteraction inside the target nucleus. An event with an η decaying into one or more π^0 's or into a γ pair at the target nucleus is also considered a signal event. Events are considered background if the final-state π^0 is only produced due to secondary interactions occurring outside of the target nucleus such as, for instance, the charge exchange of a charged pion or π^0 production in inelastic hadronic interactions. Another background category consists of the events selected accidentally, where no π^0 was produced.

According to this definition, the $\text{CC}\pi^0$ fraction predicted by the neutrino Monte Carlo, integrated over the K2K energy spectrum, is 13.9% of the total number of neutrino CC interactions. The composition of the signal is the following:

- (i) 6.5% is resonant production: 5% with a π^0 produced in the resonance decay and 1.5% with π^0 produced in a nuclear reinteraction in the target nucleus;
- (ii) 6.6% is nonresonant production, mainly DIS: 6.0% with one or more π^0 's produced at the neutrino interaction vertex and 0.6% in nuclear reinteractions in the target nucleus;
- (iii) 0.8% comes from nuclear reinteractions, mostly CC QE, where a π^0 is produced in the reinteractions in the target nucleus.

The fraction of signal events with more than one π^0 is 43%.

The final-state topology of the CC-inclusive events is characterized by one muon and at least two electromagnetic showers, plus possibly other particles coming from the neutrino interaction vertex. If the photon converts in SciBar, the hit patterns of the low-energy electromagnetic showers are reconstructed by the SciBar tracking algorithm, and the direction of the photon is given by the corresponding track. The SciBar conversion length is about 40–50 cm (SciBar, in fact, corresponds to $4 X_0$). If the photon converts in the EC, the energy is reconstructed by the EC cluster algorithm, and the position of the photon conversion is the energy-weighted average hit position in the cluster. Therefore, the experimental signature is given by one track originating in SciBar and reaching MRD and at least two photons reconstructed either as SciBar tracks disconnected and pointing to the neutrino interaction vertex or as clusters in the EC. To isolate a sample of events that satisfy the topology described above, we first select a clean sample of CC events, characterized by a SciBar track matched with an MRD track. In Sec. IV B, we describe the selection criteria to isolate the CC-inclusive sample, which is used for normalization. In the same section, we further classify CC events into subsamples of varying CC QE purities, which are used to quote the $\text{CC}\pi^0$ production cross section relative to either the CC QE or the inelastic

cross section. Out of the CC-inclusive sample, we require further cuts to select photons and to separate the CC π^0 sample from other topologies. This is described in Secs. [IV C](#) and [IV D](#). Section [IV E](#) describes the reconstruction of the incoming neutrino energy.

B. CC event selection

The selection of a CC interaction requires a muon candidate in the event. A muon candidate is a reconstructed 3D track in the SciBar fiducial volume (FV) matching a reconstructed track in the MRD. The FV is applied, requiring the upstream edge of the track to be within ± 135 cm in x and y and $-75 < z(\text{cm}) < 70$ with respect to the center of SciBar. This corresponds to a 10.9 m^3 fiducial volume and 11.6 tons of fiducial mass. The track is also required to be in time with the neutrino beam, i.e., within ± 50 ns with respect to the closest neutrino bunch. The extrapolation of the SciBar track is required to be matched with a track in MRD. The matching is with a MRD3D track or with a MRD1L hit, defined in Sec. [II B 3](#).

The neutrino interaction vertex is reconstructed as the upstream edge of the muon candidate track in SciBar. The resolution in x and y is symmetric with a 0.9-cm root mean square. The resolution in z has a 1.6-cm root mean square and a small satellite peak one SciBar layer (2.6 cm) upstream of the true neutrino vertex, due to cross talk between MAPMT channels.

We select 11 606 events in the data and 432 856 in the full MC sample (before normalization), with an estimated selection efficiency of 49.5% and a CC purity of 97.5%. The main background comes from the NC multipion or single-pion events, in which a pion gives a signal in the MRD detector. The background induced from neutrons coming from the beam target is found to be negligible.

In this analysis, we consider four CC subsamples, shown in Table [III](#), which are characterized by different fractions of non-QE (nQE) and QE interactions. The first sample consists of events with a single reconstructed track and has 72.4% efficiency and 66% purity for QE events. For the events with two tracks, the direction of the second track is compared with the expected direction of the proton in the assumption of a CC QE interaction. If this angle $\Delta\theta_p$ is smaller than 20° , the events are classified as “two-track

TABLE III. Efficiency (ϵ_{QE}) relative to all QE events selected in the CC sample, purity (η_{QE}) for QE events, and the number of events selected in MC and in data for the different QE and nQE samples.

CC subsample	$\epsilon_{\text{QE}}\%$	$\eta_{\text{QE}}\%$	Data	MC _n
1-track	72.4	66	6125	6080
2-track QE	16.9	76	1262	1307
2-track nQE π	2.3	12	1048	960
2-track nQE p	7.3	27	1453	1220

quasielastic.” Events with $\Delta\theta_p > 20^\circ$ are further divided in two categories, depending on whether the dE/dx of the second track is consistent with a pion or with a proton. The Monte Carlo is normalized to data using the first two samples in Table [III](#), which have the largest quasielastic contribution. The same normalization is used in all plots before the fit. In all plots, signal and different background components are stacked. In order to extract the result, in Sec. [V](#), we use the four samples described in Table [III](#) and we leave the data-to-MC normalization free in the fit to properly account for the correlation between the normalization and the other sources of systematic error.

C. Photon selection

All CC selected events are subject to further selection criteria to tag photons. A photon candidate can be either a SciBar track or an EC energy cluster. In order to be considered as a photon candidate, a SciBar track should satisfy the following requirements. First, the timing of the track has to be within 10 ns with respect to the muon track; second, the track is required not to be matched with a MRD3D track. Third, the photon conversion point, defined as the track edge closest to the neutrino interaction vertex, is required to be within ± 145 cm in x and y and ± 80 cm in z , with respect to the SciBar center. Fourth, in both projections, the distance between the photon conversion point and the neutrino vertex has to be larger than 20 cm; and fifth, the track extrapolation to the Z position of the neutrino vertex should be within 25 cm from the neutrino vertex. The disconnection from the vertex of SciBar photon candidates, defined as the 3D distance between the reconstructed neutrino vertex and photon conversion point, is shown in Fig. [5](#). The shape of the disconnection is consistent with MC. A fit with an exponential function between

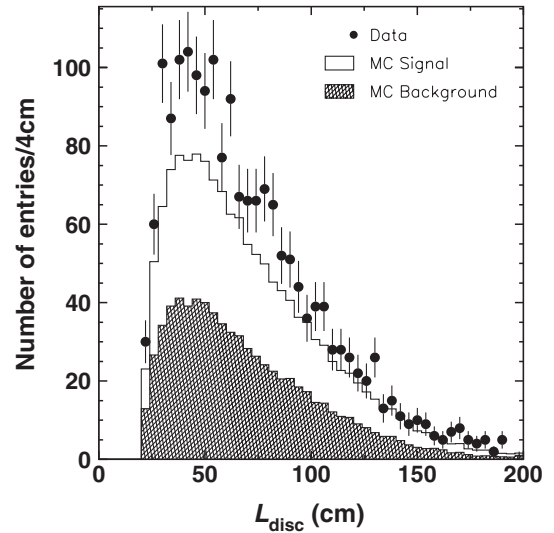


FIG. 5. Disconnection: distance L_{disc} between the reconstructed photon candidates' conversion point and the neutrino interaction vertex.

50 and 130 cm gives a value of $\lambda_{\text{disc}} = (51.8 \pm 5.4)$ cm for data, in good agreement with $\lambda_{\text{disc}} = (52.9 \pm 0.6)$ cm for MC. The result is consistent with the electromagnetic origin of the selected photon sample. In fact, according to MC, 82% of the background events also contain a genuine photon.

A fraction of photons converted in SciBar will have some energy leakage in the EC. Moreover, all the photons not converted in SciBar and pointing to the EC will convert in the upstream (vertical) EC plane. We consider only clusters with energy larger than 50 MeV for the vertical plane and 25 MeV for the horizontal plane. The energy of the SciBar photon candidates and the associated EC vertical and horizontal clusters are added together in order to reconstruct the photon energy. EC clusters that do not match any of the reconstructed SciBar tracks are considered isolated. Isolated vertical clusters are paired to isolated horizontal clusters according to their energy, and they are considered as additional photon candidates.

Overall, 479 events with at least two photons are reconstructed in data, and 380 in MC, with an overall efficiency of 7.6% and a purity of 59.2% (MC has been normalized to the data using the normalization factor described in Sec. IV B). Figure 6 shows the multiplicity of photon candidates per event.

The excess of data with respect to the MC is $26 \pm 6\%$ (statistical error only). In 74% of the candidate events, all photons are converted and reconstructed in SciBar, with possibly an energy leakage in EC. In 20% of the candidate events, one of the photons is converted and reconstructed in EC, and, in 6%, two or more photons are converted and reconstructed in EC. These relative fractions are well-reproduced by the MC. It is worth noting that this strongly supports the hypothesis that the excess of photon candidates is due to physics and not to detection bias, since SciBar and EC are completely independent detectors, with different reconstruction efficiencies and systematics.

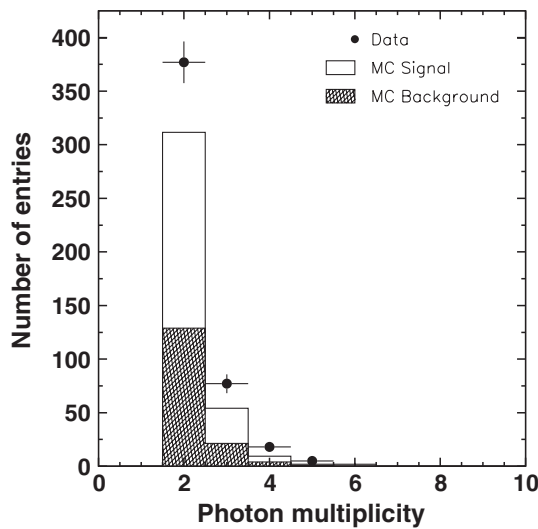


FIG. 6. Photon multiplicity of CC π^0 candidate events.

As a cross-check, we eye-scanned 100 data and 100 MC events. Despite the limited statistics and the subjectivity in the eye-scan classification criteria, the result is that the main features of the selected sample are well-reproduced by the MC simulation. In particular, the background coming from the secondary interactions in data and MC agrees within the statistical uncertainties of this eye-scan cross-check.

D. π^0 reconstruction

The π^0 mass is reconstructed from the energy and the direction of its two photon decay products:

$$M_{\pi^0} = \sqrt{2 \cdot E_{\gamma_1} \cdot E_{\gamma_2} \cdot [1 - \cos(\theta_{\gamma_1, \gamma_2})]}, \quad (1)$$

where E_{γ_1} and E_{γ_2} are the reconstructed energies of the two photons, and $\theta_{\gamma_1, \gamma_2}$ is the opening angle between them. If the photon converts in SciBar, the direction is reconstructed using the SciBar 3D reconstructed track. If the photon converts in EC, we take as the photon direction the direction of the line connecting the reconstructed neutrino vertex and the center of the EC cluster. For the highest-(lowest-) energy photon reconstructed in SciBar, the energy and angular resolutions (FWHM) are 50 (65) MeV and 0.15 (0.18) rad, respectively.

As shown in Fig. 6, in 21.4% of the selected events, there are more than two photon candidates and, therefore, more than one π^0 candidate. For these events, the photon pair corresponding to the best π^0 candidate is selected as the combination which has the reconstructed π^0 vertex closest to the neutrino interaction vertex. If there are one or more EC photon candidates (5.7% of the total sample), the best combination is selected as the photon pair with the reconstructed invariant mass closest to the π^0 mass.

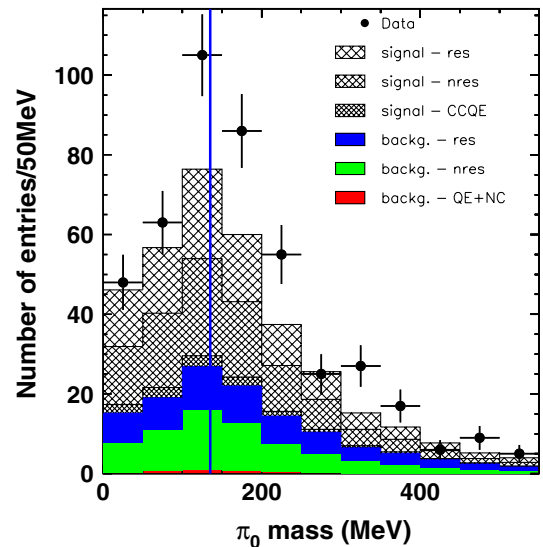


FIG. 7 (color online). Reconstructed π^0 mass before fit.

Figure 7 shows the reconstructed π^0 invariant mass for data and different MC contributions to signal and background. The signal contribution (according to the definition given in Sec. IVA) is divided into π^0 from resonant and nonresonant production and CC QE, and the background is divided into resonant and nonresonant production and CC QE, plus NC. It should be noted that most of the background contains a π^0 in the final state, so the shape of the invariant mass distribution for signal and background is similar.

E. Neutrino energy reconstruction

The neutrino energy in a CC interaction can be reconstructed from the measured muon energy and angle using the following formula, provided the invariant mass W of the hadronic final state is known:

$$E_{\nu}^{\text{rec}} = \frac{(W^2 - m_{\mu}^2) + 2E_{\mu}(M_n - V) - (M_n - V)^2}{2 \times [-E_{\mu} + (M_n - V) + p_{\mu} \cos(\theta_{\mu})]}, \quad (2)$$

where V is the nuclear potential for carbon, which is set to zero, and p_{μ} , E_{μ} , and θ_{μ} are the muon momentum, energy, and angle. For the QE final state, we have $W^2 = M_p^2$ and the formula used for neutrino energy reconstruction in the oscillation analyses. In the present analysis, 98% of the selected sample is non-QE, mostly resonant single-pion production, and DIS, and it is characterized by a broad W spectrum. We found $W = 1.483$ GeV the optimal value to reconstruct the neutrino energy in the MC sample of selected events. We use this value of W to reconstruct the neutrino energy in data and Monte Carlo. The uncertainties on the values assumed for W and for V will be considered as a source of systematic errors and evaluated in Sec. VI. The resolution turns out to be $22\%/\sqrt{E(\text{GeV})}$ for the selected sample. The assumption of an average W value is the largest effect in the reconstructed neutrino energy resolution. Using the true W value in Eq. (2), the resolution is $15\%/\sqrt{E(\text{GeV})}$.

The reconstructed neutrino energy is shown in Fig. 8 for data and different MC signal and background components. The threshold at about 1 GeV is due to the fixed value assumed for W in Eq. (2).

V. LIKELIHOOD FIT

From our sample of selected events, we measured the ratio of the inclusive CC π^0 cross section to the CC QE cross section. The uncertainties in the absolute neutrino flux cancel out in the ratio, with respect to an independent and relatively well-known process like the CC QE interaction.

We performed a maximum-likelihood fit of the reconstructed neutrino energy distribution of the CC π^0 sample shown in Fig. 8. At the same time, we fit the number of events in the different CC subsamples described in Sec. IV B. The likelihood function is defined as

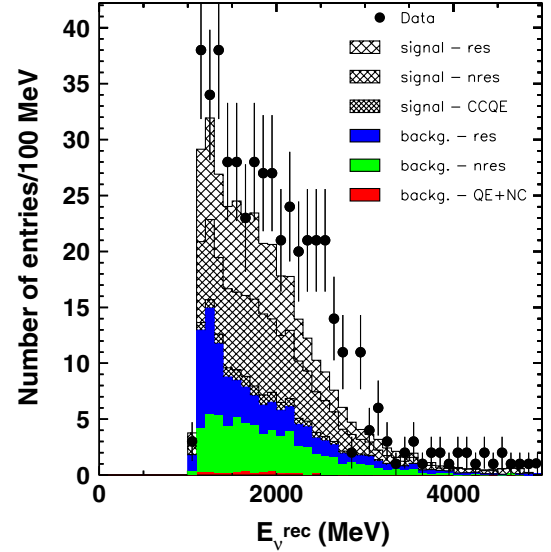


FIG. 8 (color online). Reconstructed neutrino energy before fit.

$$L = L_{\pi^0} \cdot L_{CC} = \prod_k P(n_k, \mu_k) \cdot \prod_s P(n_s, \mu_s), \quad (3)$$

where $P(n, \mu)$ is the Poisson probability for n observed events with expectation value μ . The maximum-likelihood fit is calculated by minimizing the log-likelihood function $F = -2 \log(L)$, which follows a χ^2 distribution.

The index s labels the 4 CC subsamples in Table III, and the index k labels 50 bins spanning the range 0–5 GeV of the reconstructed neutrino energy.

The expected events μ_s in each CC subsample (1-track and 2-track QE and 2-track non-QE pions and 2-track non-QE protons) are defined as

$$\mu_s = f_n \{ S_{CC,s}^{\text{QE}} + R_{\text{res}} S_{CC,s}^{\text{res}} + R_{\text{nres}} S_{CC,s}^{\text{nres}} + B_{CC,s}^{\text{NC}} \}, \quad (4)$$

where the number of Monte Carlo events contributing to signal (S_{CC}) and background (B_{CC}) are divided into QE, resonant production (res), nonresonant production (nres), and NC processes. The nonresonant production includes all non-QE CC processes different from resonant production, mainly deep inelastic scattering.

The parameters R_{res} and R_{nres} are free in the fit in order to independently reweight the corresponding Monte Carlo contributions relative to the quasielastic process.

All the MC distributions are normalized as described at the end of Sec. IV B. An additional overall normalization parameter f_n is left free in the fit.

$$\mu_k = f_n \times \left\{ \sum_j R_{CC\pi^0}(E_{\nu}^j) F_j [S_k^{\text{QE}}(E_{\nu}^j) + R_{\text{res}} S_k^{\text{res}}(E_{\nu}^j) + R_{\text{nres}} S_k^{\text{nres}}(E_{\nu}^j)] + B_k^{\text{QE}} + R_{\text{res}} B_k^{\text{res}} + R_{\text{nres}} B_k^{\text{nres}} + B_k^{\text{NC}} \right\}. \quad (5)$$

S_k and B_k are the signal and background Monte Carlo events, respectively, contributing to the final CC π^0 sample

in each bin k of reconstructed neutrino energy. The Monte Carlo signal events are further divided in 4 bins E_ν^j , according to their true neutrino energy: 0–1.5, 1.5–2.0, 2.0–2.5, and greater than 2.5 GeV. The factors F_j are defined as

$$F_j = \frac{\sum_k [S_k^{\text{QE}}(E_\nu^j) + S_k^{\text{res}}(E_\nu^j) + S_k^{\text{nres}}(E_\nu^j)]}{\sum_k [S_k^{\text{QE}}(E_\nu^j) + R_{\text{res}} S_k^{\text{res}}(E_\nu^j) + R_{\text{nres}} S_k^{\text{nres}}(E_\nu^j)],}$$

in order to keep the normalization of the signal events independent from R_{res} and R_{nres} .

The fitting parameters are $R_{\text{CC}\pi^0}(E_\nu^j)$ ($j = 1, 4$), R_{res} , R_{nres} , and f_n . The best fit of $R_{\text{CC}\pi^0}(E_\nu^j)$ gives the double ratio data over Monte Carlo between the number of inclusive $\text{CC}\pi^0$ events and the number of CC QE events, as a function of the true neutrino energy:

$$R_{\text{CC}\pi^0}(E_\nu^j) = \frac{N_{\text{CC}\pi^0}^{\text{true}}(E_\nu^j)/N_{\text{CCQE}}^{\text{true}}}{N_{\text{CC}\pi^0}^{\text{MC}}(E_\nu^j)/N_{\text{CCQE}}^{\text{MC}}}. \quad (6)$$

The scaling of the inclusive $\text{CC}\pi^0$ contribution in the fit is energy-dependent, while the energy dependence of the CC QE is fixed to the Monte Carlo prediction, since it has been accurately measured by previous experiments [51–54]. The corresponding uncertainty is considered a source of systematic error. We also performed an energy-independent fit of the $\text{CC}\pi^0$ -to-CC-QE ratio, following the same approach as Eq. (5) but with a single fit parameter $R_{\text{CC}\pi^0}$ rescaling the $\text{CC}\pi^0$ contribution, regardless of the true neutrino energy.

Table IV shows the best fit values of $R_{\text{CC}\pi^0}$ for the energy-independent fit and the four parameters $R_{\text{CC}\pi^0}(E_\nu^j)$ for the energy-dependent fit.

The $\chi^2/\text{d.o.f.}$ before the fit is $7135/44 = 162.1$. The $\chi^2/\text{d.o.f.}$ for the best fit is $40.2/37 = 1.095$ for the energy-

TABLE IV. Energy-dependent and independent fit results for $R_{\text{CC}\pi^0}(E_\nu^j)$.

Fit Variable	Fit Result
Energy-independent fit	
$R_{\text{CC}\pi^0}$	1.436 ± 0.109
R_{res}	1.152 ± 0.101
R_{nres}	1.373 ± 0.241
f_n	0.968 ± 0.025
Energy-dependent fit	
$R_{\text{CC}\pi^0}(E_\nu^1)$	1.005 ± 0.027
$R_{\text{CC}\pi^0}(E_\nu^2)$	1.180 ± 0.127
$R_{\text{CC}\pi^0}(E_\nu^3)$	1.307 ± 0.198
$R_{\text{CC}\pi^0}(E_\nu^4)$	1.418 ± 0.129
R_{res}	1.105 ± 0.098
R_{nres}	1.479 ± 0.233
f_n	0.980 ± 0.021

dependent fit and $43.8/40 = 1.089$ for the energy-independent fit.

The errors quoted for $R_{\text{CC}\pi^0}$ are purely statistical. The error induced on $R_{\text{CC}\pi^0}$ by the absolute normalization f_n and by R_{res} and R_{nres} is evaluated in the fit in order to take into account correlations but it is considered a systematic error and, together with other sources of systematic error, is discussed in Sec. VI.

Figures 9 and 10 show the reconstructed π^0 momentum and angle with respect to the beam direction in the laboratory frame, with the inclusive $\text{CC}\pi^0$ production in the Monte Carlo rescaled to the best fit value for both signal and background.

The fit results in Table IV show an excess of $\text{CC}\pi^0$ production with respect to our reference MC model. The energy-dependent fit shows that the excess increases with the neutrino energy. The data-to-MC ratio for the nonresonant processes R_{nres} is larger than 1, while the ratio for the resonant contribution R_{res} is consistent with 1, within the statistical uncertainty only. The resonant production with respect to the CC QE cross section was measured by the K2K collaboration in the $\text{CC}1\pi^+$ channel [17] and found to be $0.734^{+0.140}_{-0.153}$, in very good agreement with the MC prediction [0.740 ± 0.002 (stat)]. According to our reference MC model, 50% of the nonresonant events have one or more π^0 in the final state, and 44% of the selected $\text{CC}\pi^0$ sample is produced in nonresonant processes. Constraining the resonance production to the experimental value and uncertainty given above, we can use our $\text{CC}\pi^0$ sample to measure the nonresonant contribution.

We define CCnres (the CC nonresonant cross section) as the difference between the total CC cross section and the sum of the quasielastic and resonance productions. Using the $\text{CC}\pi^0$ sample, we perform an energy-dependent and an

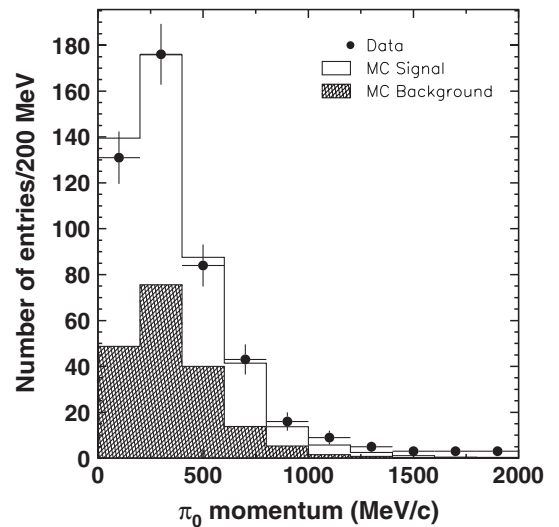


FIG. 9. π^0 momentum distribution obtained by rescaling the Monte Carlo with the energy-independent fit result.

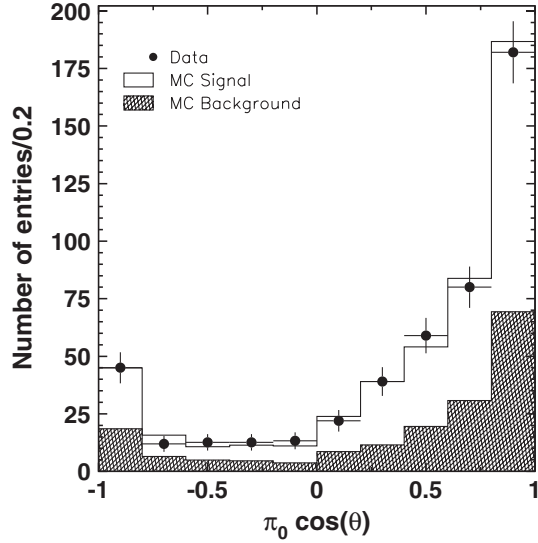


FIG. 10. $\pi^0 \cos(\theta)$ distribution obtained by rescaling the Monte Carlo with the energy-independent fit result.

energy-independent fit of the CCnres-to-CC-QE ratio, following the same approach as Eq. (5) but with $R_{CC\pi^0}$ and the normalization factors F_j fixed to one. The fit parameter R_{nres} rescaling the CC nonresonant contribution in the energy-independent fit [the parameters $R_{\text{nres}}(E_\nu^j)$ in the energy-dependent fit] and the overall normalization f_n were left free in the fit. The parameter R_{res} was also free, and the experimental constraint was incorporated in the fit by adding the term $\frac{(R_{\text{res}} - 0.99)^2}{(0.21)^2}$ to the log-likelihood function derived from Eq. (3).

Table V shows the best fit values for the energy-independent fit of R_{nres} and for the energy-dependent fit of $R_{\text{nres}}(E_\nu^j)$.

The $\chi^2/\text{d.o.f.}$ for the best fit is $41.8/39 = 1.07$ for the energy-dependent fit and $75.5/42 = 1.80$ for the energy-independent fit. The value of the $\chi^2/\text{d.o.f.}$ for the

TABLE V. Energy-dependent and independent fit results for $R_{\text{nres}}(E_\nu^j)$.

Fit Variable	Fit Result
Energy-independent fit	
R_{nres}	1.461 ± 0.118
R_{res}	1.112 ± 0.098
f_n	1.030 ± 0.012
Energy-dependent fit	
$R_{\text{nres}}(E_\nu^1)$	1.064 ± 0.266
$R_{\text{nres}}(E_\nu^2)$	0.872 ± 0.252
$R_{\text{nres}}(E_\nu^3)$	1.356 ± 0.170
$R_{\text{nres}}(E_\nu^4)$	1.567 ± 0.164
R_{res}	1.109 ± 0.102
f_n	1.026 ± 0.012

energy-independent fit shows that a three-parameter fit of signal and background, not taking into account the energy dependence of the nonresonant contributions, gives a poor description of our data.

This result is obtained by assuming that π^0 and π^+ production from resonances is constrained by the same parameter within the Rein-Sehgal model. As a consistency check, we repeated the fit without constraint to the CC π^+ measurement, and the results are consistent within 3% with the results in Table V. This difference is accounted by the systematic error, due to the uncertainty in the non-QE composition evaluated in Sec. VI.

The errors quoted for R_{nres} are purely statistical. The error induced on R_{nres} by the normalization f_n and by R_{res} is evaluated in the fit, in order to take into account correlations, but it is considered a systematic error and reported in the first row of Table VI. The full systematic error is evaluated in Sec. VI.

VI. SYSTEMATIC ERROR STUDY

In this section, we discuss the sources of systematic error. The contributors to the systematic error on the energy-independent results CC π^0 and CCnres are summarized in Table VI. The systematic errors for the energy-dependent results in Tables VII and VIII are calculated following the same approach.

TABLE VI. Systematic errors for the CC π^0 and the CC nonresonant cross sections, relative to the CC QE cross section.

Source	$\frac{\sigma_{CC\pi^0}}{\sigma_{CCQE}} [\%]$	$\frac{\sigma_{CCnres}}{\sigma_{CCQE}} [\%]$
Normalization and fit	$-1.8 + 1.8$	$-3.5 + 3.5$
Non-QE CC cross sections	$-3.4 + 3.3$	$-3.1 + 3.7$
Bodek and Yang correction	$-4.3 + 3.5$	$-8.3 + 7.8$
CC QE M_A	$-1.3 + 2.4$	$-0.8 + 1.4$
NC/CC ratio	$-0.5 + 0.5$	$-0.8 + 0.8$
ν flux	$-0.1 + 0.1$	$-0.4 + 0.4$
E_ν reconstructed parameters	$+0.2 - 0.2$	$+0.3 - 0.3$
Interaction model/flux	$-5.9 + 5.7$	$-9.6 + 9.5$
π absorption	$-2.0 + 2.1$	$-1.8 + 2.0$
π inelastic	$-3.0 + 1.8$	$-2.2 + 1.5$
Proton rescattering	$-1.9 + 0.3$	$-2.8 + 2.6$
Pion interaction length	$-1.5 + 1.5$	$-2.9 + 2.3$
Nuclear model	$-4.1 + 2.8$	$-4.9 + 4.3$
PMT resolution	$-0.5 + 0.1$	$-0.6 + 0.7$
Scintillator quenching	$-0.1 + 0.5$	$-0.4 + 0.5$
Cross talk	$+1.2 + 2.6$	$+1.4 + 2.3$
PMT threshold	$-1.7 + 2.0$	$-1.6 + 2.2$
Detector effects	$-1.8 + 3.3$	$-2.2 + 3.5$
Fiducial Volume	$-2.6 + 2.5$	$-3.3 + 3.2$
Vertex disconnection	$-1.9 + 2.4$	$-3.2 + 2.6$
Vertex pointing	$-1.0 + 1.8$	$-1.4 + 1.9$
EC cluster energy	$-0.4 + 1.2$	$-0.4 + 1.1$
Selection cuts	$-3.4 + 4.1$	$-4.8 + 4.7$
Total	$-8.1 + 8.2$	$-12.0 + 12.0$

TABLE VII. Inclusive cross section ratio $\frac{\sigma_{CC\pi^0}}{\sigma_{CCQE}}$ as a function of the neutrino energy.

Energy Range (GeV)	Cross Section Ratio ($\frac{\sigma_{CC\pi^0}}{\sigma_{CCQE}}$)
>0.0	0.426 ± 0.032 (stat) ± 0.035 (syst)
0.0–1.5	0.155 ± 0.039 (stat) ± 0.010 (syst)
1.5–2.0	0.577 ± 0.062 (stat) ± 0.037 (syst)
2.0–2.5	0.861 ± 0.130 (stat) ± 0.067 (syst)
≥ 2.5	1.627 ± 0.138 (stat) ± 0.103 (syst)

A. Interaction model and neutrino flux

The error coming from the absolute normalization for $R_{CC\pi^0}$ is estimated repeating the corresponding fit, while fixing all the other parameters, including the absolute normalization f_n at their best fit values. The resulting error for $R_{CC\pi^0}$ is the one reported in the previous section as pure statistical error, while its quadratic difference with the full fit error is reported as normalization errors in Table VI. The same procedure is applied to evaluate the errors on R_{nres} .

The systematic error coming from the uncertainty in the composition of the non-QE CC cross section has been taken into account, assigning a weight factor W_i to each non-QE CC channel and repeating the fit. A constraining function F_{syst} was added to the log likelihood derived from Eq. (3):

$$F_{syst} = \frac{\sum_i (W_i - 1)^2}{\sigma_W^2}, \quad (7)$$

where $\sigma_W = 30\%$. The double data-to-Monte-Carlo ratio of the NC-to-CC processes is also left free in the fit with a 20% constraint, adding the corresponding term to F_{syst} described in Eq. (7). The total systematic error listed in the second row of Table VI takes into account the correlation between the different sources above.

The QE axial mass is varied by $\pm 10\%$ (according to the uncertainties in the measurement reported in [55]), and the Bodek and Yang corrections to DIS events by $\pm 30\%$ [36]. The resulting systematic errors are added in quadrature in the total interaction model uncertainty.

The uncertainty in the shape of the neutrino energy spectrum shown in Fig. 1 is considered by changing the flux in each bin, taking into account their errors and the correlations between them (see Ref. [9] for details).

TABLE VIII. Cross section ratio $\frac{\sigma_{CCnres}}{\sigma_{CCQE}}$ as a function of the neutrino energy.

Energy Range (GeV)	Cross Section Ratio ($\frac{\sigma_{CCnres}}{\sigma_{CCQE}}$)
>0.0	0.419 ± 0.034 (stat) ± 0.050 (syst)
0.0–1.5	0.010 ± 0.002 (stat) ± 0.002 (syst)
1.5–2.0	0.432 ± 0.125 (stat) ± 0.056 (syst)
2.0–2.5	1.304 ± 0.164 (stat) ± 0.117 (syst)
≥ 2.5	2.954 ± 0.309 (stat) ± 0.354 (syst)

The uncertainty on the values assumed for the neutrino energy reconstruction parameters in Eq. (2) is evaluated by changing the value of $W = 1.483$ GeV by $\pm 15\%$, corresponding to assume that all non-QE selected events are from $\Delta(1232)$, rather than from an average $W = 1.483$ GeV. The nuclear potential V is varied from 0 to 27 MeV.

B. Nuclear model

Nuclear effects alter the composition and kinematics of the particles produced in neutrino interactions in nuclei.

Pion absorption and inelastic scattering processes—in particular, pion charge exchange—modify the π^0 yield. To account for the uncertainty in the Monte Carlo modeling of these effects, the pion absorption and pion inelastic scattering cross sections are varied by $\pm 30\%$ [56]. The proton rescattering is changed by $\pm 10\%$, according to the uncertainties derived from cross section measurements [56,57]. The systematic errors in Table VI are calculated by repeating the analysis for each variation of the corresponding source. The uncertainty in the pion interaction length is considered by changing its value by $\pm 20\%$. The overall uncertainty on the MC model is calculated considering the uncertainty in the pion interaction length, fully correlated to the pion inelastic cross section above.

C. Detector effects

The SciBar hit threshold, set at 2 photoelectrons, is changed by $\pm 30\%$, and the corresponding variation of the result is quoted as a systematic error.

The model for the cross talk in SciBar takes into account the second neighboring pixel and has a single free parameter n corresponding to the fraction of charge given by cross talk in the adjacent pixel. The best fit obtained, comparing data and Monte Carlo, is $n = (3.25 \pm 0.01) \times 10^{-2}$. The same model is used for the cross talk simulation in Monte Carlo and for the correction of the cross talk effect both in Monte Carlo and data. To evaluate the systematic error due to the cross talk, we changed the cross talk parameter n in the simulation in the range from 3.0 to 3.5%, corresponding to the uncertainty in the cross talk modeling[17]

Smaller systematic detector effects are induced by the uncertainties in the single photoelectron PMT resolution and the scintillator quenching (Birk's saturation) in SciBar. The SciBar PMT resolution in the Monte Carlo is set at 40% [27]. This value was chosen by tuning the dE/dx per plane for muons in Monte Carlo to match the response to cosmic-ray data. The uncertainty is evaluated to be 10%, and the corresponding systematic errors are listed in Table VI. The scintillator quenching in SciBar was measured in a beam test and is well-reproduced by Birk's equation [27]. The systematic error is evaluated by varying the Birk's parameter within its uncertainty. Other detector effects were found to give negligible contributions to the systematic error.

D. Selection cuts

In order to evaluate the systematic uncertainties due to the selection, in Table VI, we quote the dependence of the result on variations of the cuts.

We change the fiducial volume by changing (simultaneously in data and Monte Carlo), one at a time, the fiducial volume cuts in the three coordinates, according to the resolution for reconstructing the neutrino vertex: 0.8 cm for both X and Y and 1.6 cm for the Z . Then, we add in quadrature the three corresponding variations of the result.

The systematic uncertainty on the cut requiring the photon track to be disconnected from the vertex has been assessed by looking at the resolution on the neutrino vertex reconstruction and adding in quadrature the resolution on the photon conversion point. We assumed the resolution on the photon conversion point to be equal to the resolution on the muon vertex.

The cut on the photon track pointing to the vertex is applied to the distance by which the photon candidate track misses the vertex when extrapolated to the vertex plane. We take 0.14 rad for the 2D angle resolution of the photon direction (0.12 and 0.14 rad, respectively, for the most and least energetic photons). The cut is applied on photons disconnected by more than 20 cm from the vertex. They have, on average, a 50-cm distance from the vertex. We set the variation as $50 \cdot 0.14 = 7.0$ cm. In the cut region (25 cm), agreement between MC and data is quite satisfactory.

VII. RESULTS

Under the assumption that the detection efficiency is the same in data and Monte Carlo, the ratio between the inclusive $CC\pi^0$ cross section and the CC QE cross section can be calculated from Eq. (6), multiplying the best fit values of $R_{CC\pi^0}$ given in Table IV by the MC prediction for the cross section ratio in each neutrino bin E_ν^j :

$$\frac{\sigma_{CC\pi^0}}{\sigma_{CCQE}}(E_\nu^j) = R_{CC\pi^0}(E_\nu^j) \times \left[\frac{\sigma_{CC\pi^0}}{\sigma_{CCQE}}(E_\nu^j) \right]_{MC}. \quad (8)$$

Table VII shows the $CC\pi^0$ cross section ratio to CC QE, integrated over all energies and as a function of the four neutrino energy bins. Figure 11 shows the result as a function of neutrino energy. The vertical bars are the statistical errors, the height of the filled areas corresponds to the statistical and systematic errors added in quadrature, and the data points in each bin are set at the weighted averages of the true neutrino energy for the selected $CC\pi^0$ events. Figure 11 also shows the $CC\pi^0$ -over-CC-QE ratio and the two largest contributions, single pions from resonances and pions produced in DIS, as they are predicted by our reference MC. According to our reference MC, the average true neutrino energy for the selected CC QE events is 1.1 GeV. The average true neutrino energy for our selected π^0 sample is 1.3 and 2.5 GeV for the fraction of π^0 produced in DIS events.

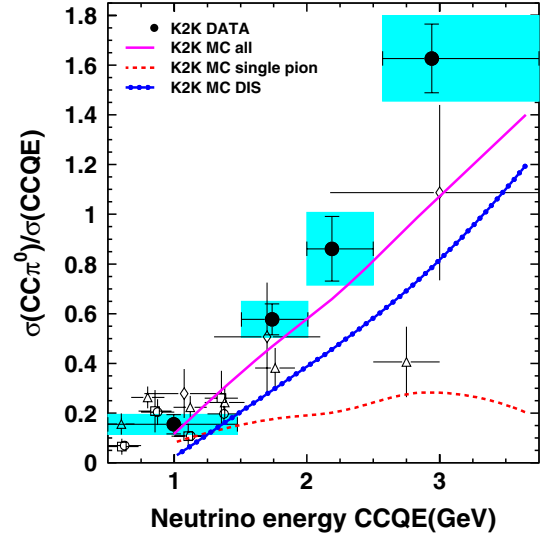


FIG. 11 (color online). $CC\pi^0$ -to-CC-QE cross section ratio as a function of neutrino energy. The result of this analysis (\bullet) is compared with our standard MC expectation and past experimental results. The previous experimental data are: (\circ) ANL82 [11], (\square) ANL [51], (\triangle) BNL86 [12], and (\diamond) ANL83 + BNL86 [12,14] (see text for details).

The CC-nonresonant-to-CC-QE ratio is obtained from the best fit values of R_{nres} in Table V, similarly to Eq. (8):

$$\frac{\sigma_{CCnres}}{\sigma_{CCQE}}(E_\nu^j) = R_{nres}(E_\nu^j) \times \left[\frac{\sigma_{CCnres}}{\sigma_{CCQE}}(E_\nu^j) \right]_{MC}. \quad (9)$$

The results for $\frac{\sigma_{CCnres}}{\sigma_{CCQE}}$ are reported in Table VIII, integrated over all energies and as a function of the four neutrino energy bins.

Comparison with other experiments

Past experimental results exist for the exclusive $\nu_\mu n \rightarrow \mu^- p \pi^0$ cross sections on deuterium (Barish [10], Radecky [11], and Kitagaki [12]). There is also a published result for the exclusive cross section $\nu + p \rightarrow \mu^- p \pi^+ \pi^0$ (Day [14]). In order to compare with our result on C_8H_8 , cross sections on deuterium have been rescaled to the different number of protons and neutrons. The ratio between $CC\pi^0$ and CC QE cross sections is computed by dividing the experimental results quoted above by the CC QE cross section measured by Barish [51]. Below 1.5-GeV neutrino energy, our result can be directly compared with the published single-pion cross sections, since this is the main contribution to the inclusive cross section. The three points shown as diamond-shaped symbols at 1.07, 1.70, and 3.0 GeV are obtained adding the two-pion $\mu^- p \pi^+ \pi^0$ from [14] to the single pions $\mu^- p \pi^0$ taken from [12].

The MiniBooNE collaboration has recently published charged-current π^0 production [58] at a slightly lower neutrino energy (between 0.5 and 2 GeV), and their result is consistent with the one presented in this paper.

VIII. CONCLUSION

Out of a sample of 11 606 charged-current neutrino interactions in the K2K SciBar detector, we selected 479 inclusive π^0 events with an efficiency of 7.8% and a purity of 66.5%. The sample corresponds to 2.02×10^{19} protons on target recorded with the SciBar + EC + MRD detectors at 1.3-GeV average beam neutrino energy. We measured the cross section for charged-current π^0 production relative to the charged-current quasielastic cross section to avoid the large uncertainties in the absolute neutrino flux determination. The result integrated over the neutrino energy spectrum is

$$\frac{\sigma_{CC\pi^0}}{\sigma_{CCQE}} = 0.426 \pm 0.032 \text{ (stat)} \pm 0.035 \text{ (syst)},$$

higher than the prediction of our reference Monte Carlo. The energy-dependent CC π^0 -to-CC-QE cross section ratio is presented in Table VII and shown in Fig. 11. The results of the best fit for the composition of our CC π^0 sample show that the data excess comes from nonresonant processes, mainly π^0 production in DIS, rather than from π^0 in resonance production. Using the measured CC single charged pion cross section [17] as a constraint for the resonant production, we measured the ratio between the CC nonresonant and the CC QE cross section, integrated over the neutrino energy spectrum:

$$\frac{\sigma_{CCnres}}{\sigma_{CCQE}} = 0.419 \pm 0.034 \text{ (stat)} \pm 0.050 \text{ (syst)}.$$

For CC nonresonant processes, we define any charged-current process, except quasielastic interaction and resonance production. The energy-dependent cross section ratio is presented in Table VIII. The results presented here are the first for neutrinos of few-GeV energy on C₈H₈ target material, improve the precision of previous results on different targets, and, therefore, are a significant contribution to the knowledge of neutrino interaction processes relevant for several present and future oscillation experiments.

ACKNOWLEDGMENTS

We thank the KEK and ICRR directorates for their strong support and encouragement. K2K was made possible by the inventiveness and the diligent efforts of the KEK-PS machine group and beam channel group. We gratefully acknowledge the cooperation of the Kamioka Mining and Smelting Company. This work has been supported by the Ministry of Education, Culture, Sports, Science, and Technology of the Government of Japan, the Japan Society for Promotion of Science, the U.S. Department of Energy, the Korea Research Foundation, the Korea Science and Engineering Foundation, NSERC Canada and the Canada Foundation for Innovation, the Istituto Nazionale di Fisica Nucleare (Italy), the Ministerio de Educaci3n y Ciencia and Generalitat Valenciana (Spain), the Commissariat à l'Énergie Atomique (France), and Polish KBN Grants No. 1P03B08227 and No. 1P03B03826.

-
- [1] Raymond Davis, *Phys. Rev. Lett.* **12**, 303 (1964).
 - [2] Y. Fukuda *et al.*, *Phys. Rev. Lett.* **77**, 1683 (1996).
 - [3] W. Hampel *et al.*, *Phys. Lett.* **447B**, 127 (1999).
 - [4] J.N. Abdurashitov *et al.*, *Phys. Rev. C* **60**, 055801 (1999).
 - [5] Y. Fukuda *et al.*, *Phys. Rev. Lett.* **81**, 1158 (1998).
 - [6] Q.R. Ahmad *et al.*, *Phys. Rev. Lett.* **87**, 071301 (2001).
 - [7] Y. Fukuda *et al.*, *Phys. Rev. Lett.* **81**, 1562 (1998).
 - [8] T. Araki *et al.*, *Phys. Rev. Lett.* **94**, 081801 (2005).
 - [9] M.H. Ahn *et al.*, *Phys. Rev. D* **74**, 072003 (2006).
 - [10] S.J. Barish *et al.*, *Phys. Rev. D* **19**, 2521 (1979).
 - [11] G.M. Radecky *et al.*, *Phys. Rev. D* **25**, 1161 (1982).
 - [12] T. Kitagaki *et al.*, *Phys. Rev. D* **34**, 2554 (1986).
 - [13] T. Kitagaki *et al.*, *Phys. Rev. D* **42**, 1331 (1990).
 - [14] D. Day *et al.*, *Phys. Rev. D* **28**, 2714 (1983).
 - [15] D. Allasia *et al.*, *Nucl. Phys.* **B343**, 285 (1990).
 - [16] H.J. Grabosch *et al.*, *Z. Phys. C* **41**, 527 (1989).
 - [17] A. Rodriguez *et al.*, *Phys. Rev. D* **78**, 032003 (2008).
 - [18] E. Aliu *et al.*, *Phys. Rev. Lett.* **94**, 081802 (2005).
 - [19] M.H. Ahn *et al.*, *Phys. Rev. Lett.* **90**, 041801 (2003).
 - [20] S.H. Ahn *et al.*, *Phys. Lett. B* **511**, 178 (2001).
 - [21] S. Nakayama *et al.*, *Phys. Lett. B* **619**, 255 (2005).
 - [22] A. Suzuki *et al.*, *Nucl. Instrum. Methods Phys. Res., Sect. A* **453**, 165 (2000).
 - [23] K. Nitta *et al.*, *Nucl. Instrum. Methods Phys. Res., Sect. A* **535**, 147 (2004).
 - [24] S. Yamamoto *et al.*, *IEEE Trans. Nucl. Sci.* **52**, 2992 (2005).
 - [25] A. Pla-Dalmau (MINOS Scintillator Group), *Frascati Phys. Ser.* **21**, 513 (2001).
 - [26] M. Yoshida *et al.*, *IEEE Trans. Nucl. Sci.* **51**, 3043 (2004).
 - [27] M. Hasegawa, PhD thesis, Kyoto University, 2006.
 - [28] A. Glazov, I. Kisel, E. Konotopskaya, and G. Ososkov, *Nucl. Instrum. Methods Phys. Res., Sect. A* **329**, 262 (1993).
 - [29] S. Buontempo *et al.*, *Nucl. Instrum. Methods Phys. Res., Sect. A* **349**, 70 (1994).
 - [30] D. Acosta *et al.*, *Nucl. Instrum. Methods Phys. Res., Sect. A* **294**, 193 (1990).
 - [31] T. Ishii *et al.*, *Nucl. Instrum. Methods Phys. Res., Sect. A* **482**, 244 (2002).
 - [32] Y. Hayato, *Nucl. Phys. B, Proc. Suppl.* **112**, 171 (2002).

- [33] Dieter Rein and Lalit M. Sehgal, *Ann. Phys. (N.Y.)* **133**, 79 (1981).
- [34] D. Rein, *Z. Phys. C* **35**, 43 (1987).
- [35] M. Gluck, E. Reya, and A. Vogt, *Z. Phys. C* **67**, 433 (1995).
- [36] A. Bodek and U. K. Yang, *Nucl. Phys. B, Proc. Suppl.* **112**, 70, (2002).
- [37] Masayuki Nakahata *et al.*, *J. Phys. Soc. Jpn.* **55**, 3786 (1986).
- [38] Torbjorn Sjostrand, *Comput. Phys. Commun.* **82**, 74 (1994).
- [39] R. A. Smith and E. J. Moniz, *Nucl. Phys.* **B43**, 605 (1972).
- [40] E. J. Moniz *et al.*, *Phys. Rev. Lett.* **26**, 445 (1971).
- [41] S. K. Singh, M. J. Vicente-Vacas, and E. Oset, *Phys. Lett. B* **416**, 23 (1998).
- [42] C. H. Llewellyn Smith, *Phys. Rep.* **3**, 261 (1972).
- [43] Dieter Rein and Lalit M. Sehgal, *Nucl. Phys.* **B223**, 29 (1983).
- [44] M. Hasegawa *et al.*, *Phys. Rev. Lett.* **95**, 252301 (2005).
- [45] Roger D. Woods and David S. Saxon, *Phys. Rev.* **95**, 577 (1954).
- [46] L. L. Salcedo, E. Oset, M. J. Vicente-Vacas, and C. Garcia-Recio, *Nucl. Phys.* **A484**, 557 (1988).
- [47] Glenn Rowe, Martin Salomon, and Rubin H. Landau, *Phys. Rev. C* **18**, 584 (1978).
- [48] C. W. Walter, *Nucl. Phys. B, Proc. Suppl.* **112**, 140 (2002).
- [49] R. Brun *et al.*, CERN Report No. CERN-DD/EE/84-1, 1987.
- [50] C. Zeitnitz and T. A. Gabriel, *Nucl. Instrum. Methods Phys. Res., Sect. A* **349**, 106 (1994).
- [51] S. J. Barish *et al.*, *Phys. Rev. D* **16**, 3103 (1977).
- [52] S. Bonetti *et al.*, *Nuovo Cimento Soc. Ital. Fis. A* **38**, 260 (1977).
- [53] S. Ciampolillo *et al.*, *Phys. Lett.* **84B**, 281 (1979).
- [54] S. V. Belikov *et al.*, *Z. Phys. A* **320**, 625 (1985).
- [55] R. Gran *et al.*, *Phys. Rev. D* **74**, 052002 (2006).
- [56] C. H. Quentin Ingram *et al.*, *Phys. Rev. C* **27**, 1578 (1983).
- [57] E. J. Jeon, PhD thesis, The Graduate University for Advanced Studies (Sokendai), 2003.
- [58] A. A. Aguilar-Arevalo *et al.*, arXiv:hep-ex/1010.3264.
- [59] N. Armenise *et al.*, *Nucl. Phys.* **B152**, 365 (1979).
- [60] Priscilla S. Auchincloss *et al.*, *Z. Phys. C* **48**, 411 (1990).
- [61] J. P. Berge *et al.*, *Z. Phys. C* **35**, 443 (1987).
- [62] V. B. Anikeev *et al.*, *Z. Phys. C* **70**, 39 (1996).
- [63] A. I. Mukhin *et al.*, *Sov. J. Nucl. Phys.* **30**, 528 (1979).
- [64] D. MacFarlane *et al.*, *Z. Phys. C* **26**, 1 (1984).
- [65] N. J. Baker *et al.*, *Phys. Rev. D* **25**, 617 (1982).